(Received 17 December 2024, Accepted 24 January 2025, Scheduled 3 February 2025)

Comparison and Analysis of Dual-Stator Magnetic Field Modulation Motors with Different Permanent Magnet Arrangements

Libing Jing, Tao Wang, Zeyu Min*, and Weizhao Tang

College of Electrical Engineering and New Energy, Hubei Provincial Engineering Technology Research Center for Microgrid China Three Gorges University, Yichang 443002, China

ABSTRACT: The Double Stator Magnetic Field Modulation Motor (DSMFMM) realizes the magnetic field modulation effect and optimizes the torque ripple effect by accurately optimizing the flux line. In order to further explore the influence of permanent magnets (PMs) magnetization model on the performance of DSMFMM, this paper conducts a comparative study on the performance of three motors with radial magnetization, Halbach magnetization, and Spoke magnetization. Firstly, three motor models are designed based on the same outer radius and axial length, and the flux lines of the three motors are analyzed in detail. Secondly, the static and dynamic performances of the three models are compared by finite element analysis (FEA) method. Compared with the conventional radial magnetization structure, the DSMFMM structure with Halbach magnetization and Spoke magnetization improves the output torque and torque density of the motor.

1. INTRODUCTION

With the rapid advancement of modern industrial technology, the motor has become a key device for transforming electrical energy into mechanical energy [1–3]. The optimization of motor performance and the improvement of efficiency have attracted wide attention from academia and industry. It is worth noting that high-performance motors play a vital role in areas such as high-precision control, energy conservation and emission reduction, and renewable energy utilization [4–6].

Conventional motors need to be connected to the drive shaft, which increases the volume and weight of the motor [7, 8]. The permanent magnet synchronous motor simplifies the structure by direct connection, making the motor lighter and more compact. However, the permanent magnet synchronous motor has magnetic flux leakage during operation [9]. Therefore, from the perspective of optimizing the flux line and proposing a new topology, there is still room for improvement in motor performance.

In recent years, scholars have carried out many studies on optimizing the flux line of the motor. Adding stator structure to the inner and outer rotors of the convention motor is an effective method to optimize the flux line. In [10], a double-stator permanent magnet synchronous is proposed. By properly adjusting the winding of the inner and outer windings, the motor has higher torque and power density. In [11], a new design strategy centers on the power level to calculate the size of the double-stator switched reluctance motor. The inner and outer rotor motors are designed respectively, and then the results are combined together.

In order to further utilize the effective flux line and increase the torque, magnetic field modulation motor has become one of the powerful candidates [12]. It regulates the magnetic field inside the motor through a specific magnetic field modulation structure to achieve high efficiency and high precision operation of the motor. In [13, 14], the optimal design and control strategy of a new type of double-stator magnetic field modulated motor were studied in depth. In addition, the application prospects and potential advantages of dual-stator magnetic field modulated motors were discussed [15].

However, these studies did not involve the influence of permanent magnet magnetization on the performance of the motor. In this paper, the magnetic field modulation theory is integrated into the motor design, and three motor topologies are proposed according to the different magnetizations of permanent magnets. Then, the three motor structures are compared in detail from the perspectives of torque output capability, torque, power density, and operating efficiency, and the performance and characteristics of different topologies are analyzed.

The organization of this paper is outlined as follows. In the first part, the DSMFMM structure with conventional radial magnetic field is briefly introduced. Then, combined with different permanent magnet magnetization structures, two new Spoke and Halbach DSMFMM structures are proposed, and the magnetic flux line of the motor is analyzed. Subsequently, two novel DSMFMM structures with spoke and Halbach configurations are proposed. The flux lines of these motors are analyzed. In the second part, the general design procedure for the motor is provided, and the motor is designed under the same inner and outer diameter and axial length parameters. In the third part, the performances of the three motors are compared and ana-

* Corresponding author: Zeyu Min (minzeyu@ctgu.edu.cn).

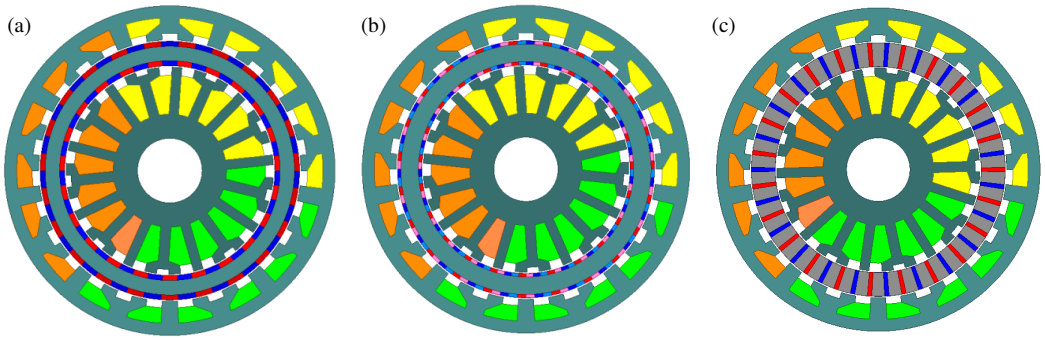

FIGURE 1. Topologies of DSMFMs. (a) M1: with radial PMs. (b) M2: with Halbach PMs. (c) M3: with spoke-array PMs.

lyzed in detail, including magnetic density, flux linkage, and torque characteristics. Simulations for steady-state and starting conditions of the motors are conducted. In the end, conclusions are drawn in this paper.

2. TOPOLOGY AND OPERATION PRINCIPLE

Figure 1 shows the three DSMFMM models, which are marked as M1, M2, and M3, respectively, corresponding to radially magnetized PM, Halbach PM, and spoke array PM. The common feature of these three motors is that the inner stator has 9 slots, which are occupied by three-phase concentrated windings.

Each stator tooth of the motors is divided into two flux-modulating poles, with isolation teeth inserted for inter-phase separation. The introduction of auxiliary teeth and modulation teeth not only play the role of magnetic field modulation, but also play the role of phase isolation. This enhances the output torque of the motor and improves the stability of the motor. The stator includes 27 flux-modulating poles. This signifies that the pole pair combinations of flux-modulating pole (FMP), PM, and winding poles for the three motors are 27/23/4, respectively. When the slots per pole per phase exceed 1/2, the double-layer winding structure exhibits a relatively high fundamental winding factor. Consequently, the proposed motors M1, M2, and M3 with the 27/23/4 combinations adopt a double-layer winding connection.

Assuming that the initial angle of the target motor is zero, through the three-phase symmetrical sinusoidal current, the three-phase synthetic magnetomotive force calculation formula is expressed as:

$$F_c = \frac{6\sqrt{2}NI}{\pi p}\sum\nolimits_k^{\infty}\left\{\frac{1}{6k+1}\sin\frac{(6k+1)\pi}{2}\sin\frac{(6k+1)\pi}{6}\right.$$
$$\left.\cdot\cos\left[(6k+1)p\omega_r t-(6k+1)\right]p\theta\right\} \tag{1}$$

where $k=0,\pm1,\pm2\cdots I$ is the effective value of each phase current (A); N is the winding turns of each phase; p is the pole-pair number; θ is the mechanical angle (°); ω_r is the rotor speed.

The permeability of the stator up-regulated magnetic tooth modulation pole is

$$\Lambda=\Lambda_1+\sum_{j=1,2,3,\ldots}^{\infty}\Lambda_j\cos\left(jn_s\theta\right) \tag{2}$$

where n_s is the number of pole; Λ_j is the amplitude of the jth harmonic permeance.

According to the above two formulas, the radial air gap flux density after harmonic magnetic field modulation can be expressed as:

$$B_r(r,\theta)=F_c\Lambda=\Lambda_1\frac{6\sqrt{2}NI}{\pi p_1}\sum_k^{\infty}\left\{\frac{1}{6k+1}\sin\frac{(6k+1)\pi}{2}\right.$$
$$\left.\sin\frac{(6k+1)\pi}{6}\cos\left[C_0-(6k+1)\right]p\theta\right\}+\frac{1}{2}\sum_{j=1,2,3,\ldots}^{\infty}\sum_k^{\infty}$$
$$\frac{1}{6k+1}\sin\frac{(6k+1)\pi}{2}\sin\frac{(6k+1)\pi}{6}\Lambda_j F_0\cos\left[C_1\left(\theta\right.\right.$$
$$\left.\left.-\frac{(6k+1)p\omega_r t}{C_1}\right)\right]+\frac{1}{2}\sum_{j=1,2,3,\ldots}^{\infty}\sum_k^{\infty}\frac{1}{6k+1}\sin\frac{(6k+1)\pi}{2}$$
$$\sin\frac{(6k+1)\pi}{6}\Lambda_j F_0\cos\left[C_2\left(\theta-\frac{(6k+1)p\omega_r t}{C_2}\right)\right] \tag{3}$$

$$\begin{cases}C_0=(6k+1)p\omega_r t\\ C_1=-(6k+1)p+jn_s\\ C_2=-(6k+1)p-jn_s\end{cases} \tag{4}$$

The number of poles of the magnetic field on the stator armature can be obtained as follows:

$$p_{-(6k+1),k}=\left|-(6k+1)p+in_s\right|,\quad i=0,\pm1,\pm2\cdots \tag{5}$$

The relationship among the number of magnetic teeth, the number of stator armature, and the number of rotor poles is obtained as follows:

$$p_{i,m,k}=\left|mp_i+in_s\right|,\ m=1,3,5\cdots;\ i=0,\pm1,\pm2\cdots \tag{6}$$

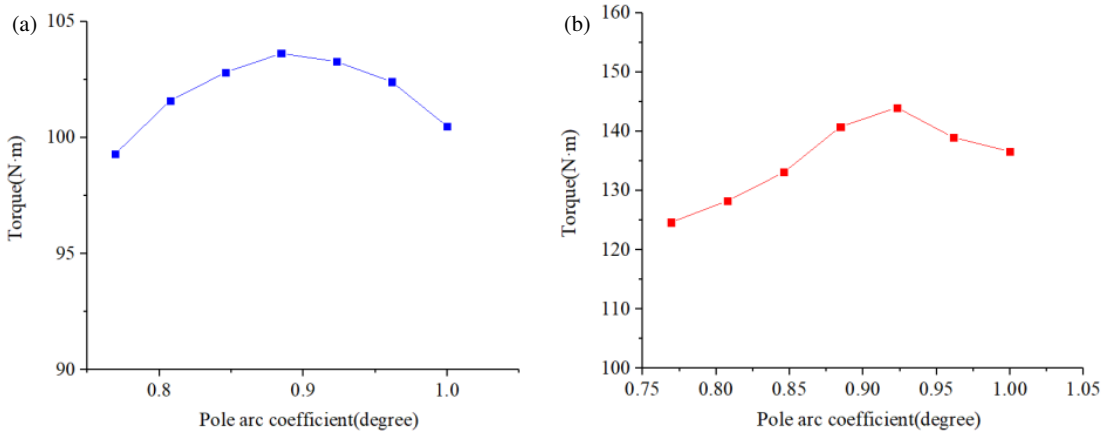

FIGURE 2. The relationship between pole arc coefficient and torque. (a) M1. (b) M2.

where p_i is the number of stator armature poles; $p_{i,m,k}$ is the rotor pole pairs; n_s is the number of magnetic teeth.

The rotational angular velocity of the spatial magnetic field harmonics after modulation is expressed as:

$$\omega_r = \frac{mp}{mp + kn_s}\omega_s \tag{7}$$

where ω_r is the rotor speed; ω_s is the Stator armature magnetic field speed.

Based on this unique magnetic field modulation, the output torque can be transmitted through the air gap fundamental wave and effective harmonic field. Its speed ratio is expressed as:

$$G_r = -\frac{\omega_s}{\omega_r} = \frac{p - p_s}{p} \tag{8}$$

3. MOTOR ANALYSIS AND OPTIMIZATION

Factors impacting the air gap flux density of DSMFMM fall into two categories: conventional motor parameters and repulsion factors. Conventional motor parameters include air gap length, pole arc coefficient, and PM thickness. Repulsion factors, arising from the integration of flux modulation plates at the stator teeth, encompass FMP width and gear ratio. To maintain comparison fairness, designed prototypes must share uniform core material, inner and outer diameters, axial length, bus voltage, and speed. However, due to their unique designs, slight differences are observed in stator yoke height, stator pole length, rotor pole length, stator slot width, and rotor slot width.

3.1. The Impact of the Pole Arc Coefficient on Output Torque

The pole arc coefficient indicates the variation in permanent magnet (PM) volume, influencing the air-gap flux density distribution. In both surface-mounted and Halbach DSMFMMs (M1 and M2), the pole arc coefficient (α_p) is defined as the ratio of pole arc width (τ_w) to pole pitch (τ), aligning with traditional DSMFMMs.

Figure 2 show the relationship between torque and pole arc coefficient of the two machines. As can be seen from Fig. 2, we can observe that the torque decreases first and then increases with the increase of the pole arc coefficient.

3.2. The Influence of PM Thickness on Output Torque

For the proposed DSMFMMs of M1 and M2, there are no definitive constraints linking αp and PM thickness. Consequently, PM thickness can be varied freely within the rotor radius. However, under a fixed rotor radius, a correlation exists between PM thickness and performance.

Figure 3 illustrates how the output torques of M1 and M2 change with PM thickness. As can be seen from Fig. 3, with the increase of PM thickness, the torques of both M1 and M2 will increase. However, when PM thickness exceeds 2 mm, the growth rate of output torque becomes very slow.

It is noteworthy that the α_p of M3 diminishes as the PM thickness increases, provided that the PM pole-pair number and pole pitch (τ) remain constant. Additionally, variations in PM pole-pair number further influence α_p, which is then constrained not solely by PM thickness but also by PM pole-pair number.

For the spoke-array DSMFMM of M3, the pole arc width and pole pitch are denoted as τ_0 and 2τ, as shown in Fig. 4. The corresponding pole arc coefficient α_p of M3 is defined as

$$\alpha_p = \frac{\tau_0}{2\tau} \tag{9}$$

Figure 5 shows the relationship between rotor torque and PM thickness of M3. As can be seen from Fig. 6, with the increase of PM thickness, the torques of both M1 and M2 will increase. However, when PM thickness exceeds 2 mm, the growth rate of output torque becomes very slow.

Table 1 outlines their electrical and structural specifications.

4. PERFORMANCE ANALYSIS AND COMPARISON

Under the premise of identical structural dimensions, core materials, phase voltages, and speeds for the three models, a comparative analysis is conducted on their static and dynamic per-

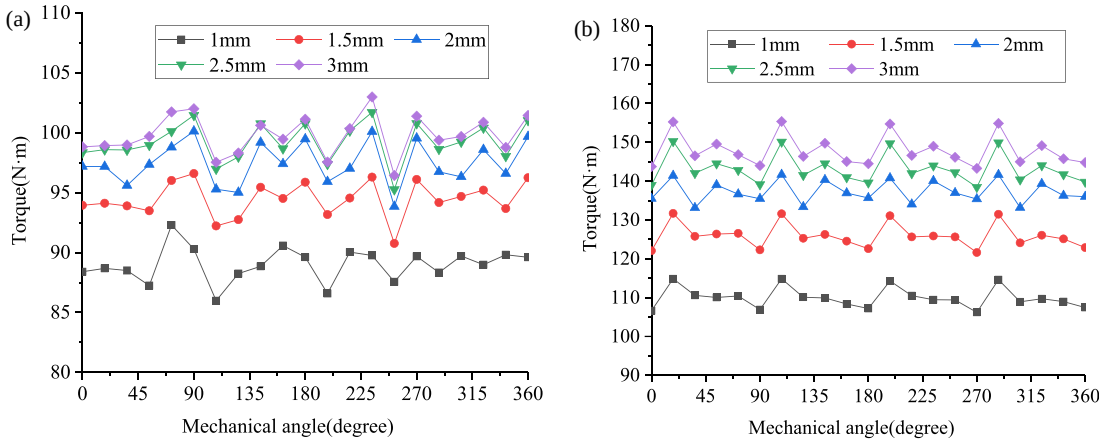

FIGURE 3. The variations of the output torque of PM thickness. (a) M1. (b) M2.

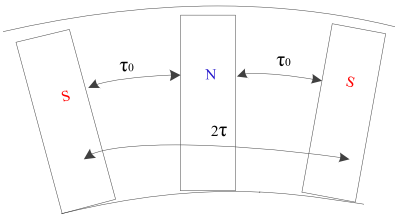

FIGURE 4. Illustration of pole arc width and pole pitch of M3.

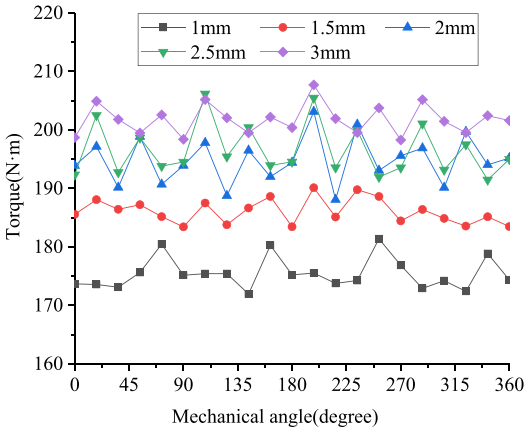

FIGURE 5. The relationship between rotor torque and PM thickness of M3.

formances. It includes static flux density characteristics, static torque characteristics, flux linkage characteristics, inductance characteristics, and steady-state operation characteristics.

4.1. Static Performance Comparison

The electromagnetic performance of the motor serves as a crucial benchmark for assessing its overall performance. In this part, the electromagnetic characteristics of the target motor are examined using the finite element method. Firstly, according to the structural size parameters of Table 1, the FEA of three models was established in Ansys Maxwell software.

The magnetic flux density of the motor under no-load condition is shown in Fig. 6. It can be seen that in the no-load state of

TABLE 1. Main specification.

	M1	M2	M3
Number of rotor pole	23	23	23
Armature pole pairs	4	4	4
Slot number	9	9	9
Outer radius of outer stator	102 mm	102 mm	102 mm
Inner radius of outer stator	81 mm	81 mm	81 mm
PM length	2 mm	15 mm	2 mm
Outer radius of inner stator	64 mm	64 mm	64 mm
Inner radius of inner stator	20 mm	20 mm	20 mm
Axial length	100 mm	100 mm	100 mm
Air gap	1 mm	1 mm	1 mm
PM material	NdFe35	NdFe35	NdFe35

the motor, 4 pairs of pole magnetic fields are generated on the inner stator and outer stator, and 23 pairs of pole magnetic fields are generated on the permanent magnet on the rotor, which satisfies the corresponding relationship in Eq. (6). Since M3 uses spoke array magnet to obtain flux focusing effect, the air gap flux density has been greatly improved.

Figure 7 depicts the distribution of flux density in the outer air gap. According to the principle of magnetic field modulation, the harmonic components with pole pairs of 4, 23, 31, and 50 are identified as the operational harmonics. Observation reveals that the radial air gap magnetic flux density amplitude in the M3 motor model is marginally higher than the M1 and M2 motor models. Furthermore, the amplitude in the M2 motor model is slightly greater than that in the M1 model. This is attributed to the efficient utilization of flux lines achieved through spoke and Halbach magnetization techniques.

Figure 8 displays the flux density waveform of the inner air gap. By altering the structure of the permanent magnet, it becomes evident from the diagram that the radial air gap magnetic density waveform of the M2 and M3 is larger than that of M1. In comparison to the M1 model, the non-working harmonics of the 12th, 20th, 28th, and 36th orders in the M2 model are significantly suppressed. This contributes to reducing the torque ripple of the motor and enhancing its stability. Furthermore, compared to M1 model, M3 model optimizes the flux line, re-

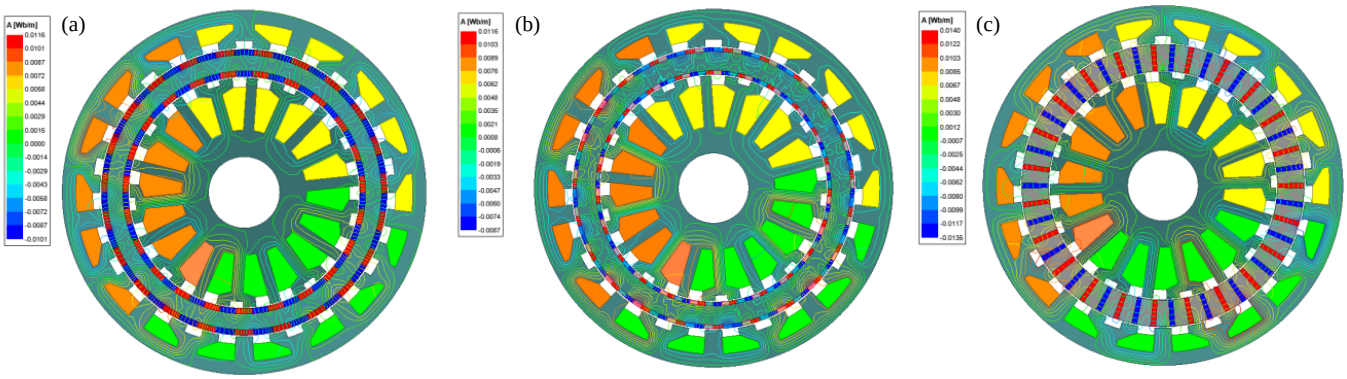

FIGURE 6. Flux density. (a) M1, (b) M2, and (c) M3.

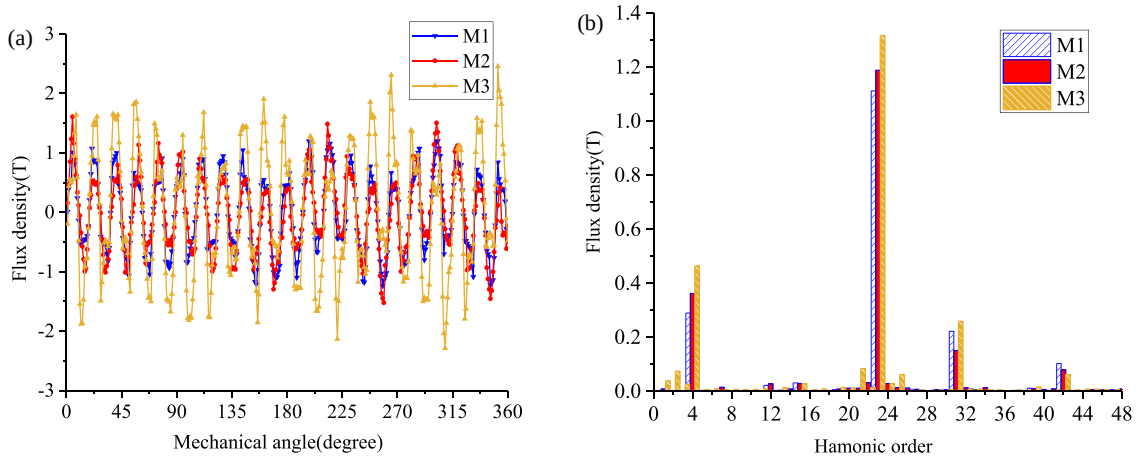

FIGURE 7. Flux density in the outer air gap. (a) Flux density; (b) Harmonic order.

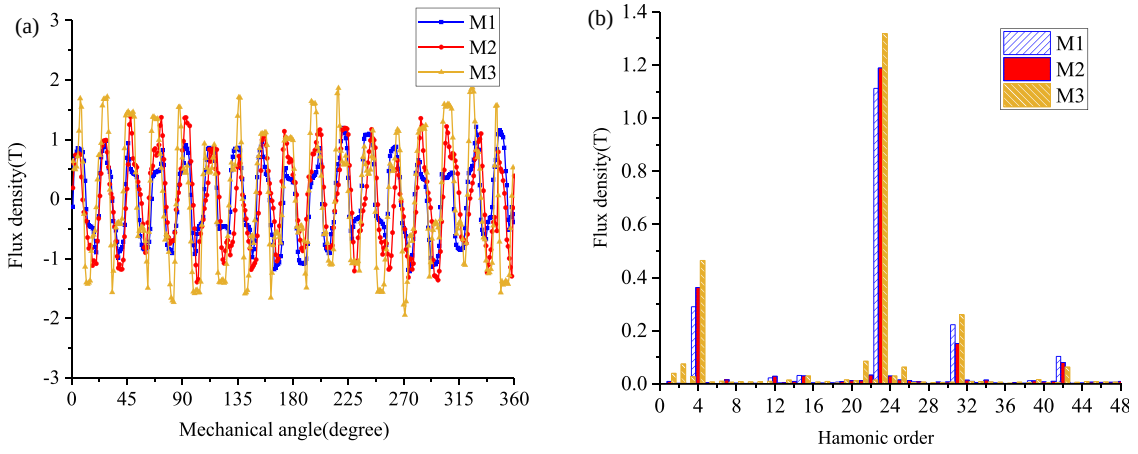

FIGURE 8. Flux density in the inner air gap. (a) Flux density; (b) Harmonic order.

sulting in an improved air gap flux density and a higher output torque.

4.2. Analysis of No-Load Back Electromotive Force

The harmonic distortion rate of the no-load back-EMF of the motor is one of the standards to characterize the operation stability of the motor. When the distortion rate is smaller, the actual operation of the motor is more stable. Its calculation formula is as follows:

$$THD = \frac{\sqrt{\sum_{i=2}^{n} B_{\delta i}^2}}{B_{\delta 1}} \times 100\% \tag{10}$$

where THD is the harmonic total distortion rate; $B_{\delta 1}$ is the magnitude of the air gap magnetic flux density's fundamental wave;

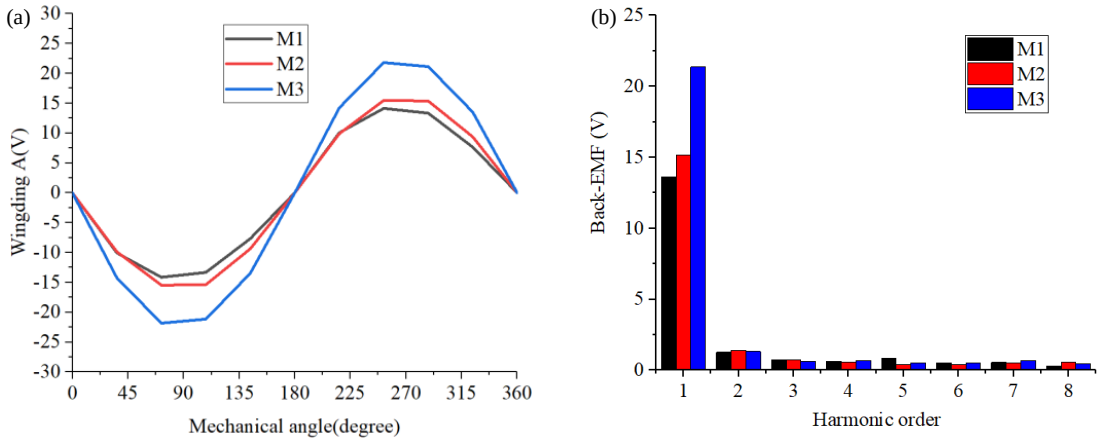

FIGURE 9. Back-EMF. (a) Waveform; (b) Harmonic order.

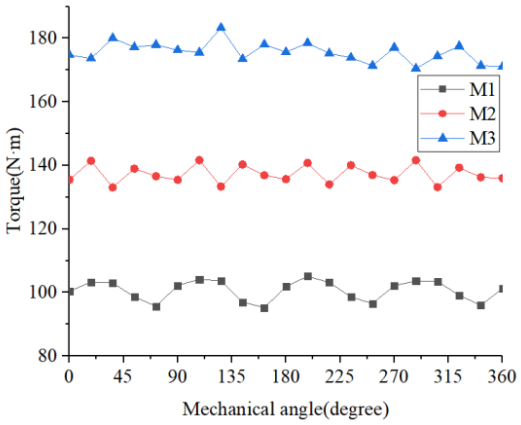

FIGURE 10. Electromagnetic torque.

$B_{\delta i}$ is the magnitude of the ith harmonic air gap magnetic flux density.

Taking phase A of the three-phase winding of DSMFMM as an example, the no-load back EMF and harmonics of the phase A armature winding are analyzed, as shown in Fig. 9. Obviously, the waveforms of the three curves are in the form of sine waves, as shown in Fig. 9(a). A period of the back electromotive force is taken for harmonic analysis, as shown in Fig. 9(b). It was found that the fundamental electromotive force amplitudes of the three motors were 13.63 V, 15.18 V, and 21.37 V, respectively. According to formula (10), the total harmonic distortion rates of no-load back EMF are 5.97%, 48%, and 4.45%, respectively, which proves that the harmonic content of no-load back EMF is less, and the motor operation is more stable.

4.3. Torque Analysis

According to Maxwell stress tensor method, when the axial length remains constant, the electromagnetic torque is directly proportional to the product of radial magnetic density and tangential magnetic density. The torque expression is as follows:

$$T_{em} = \frac{L_{ef} R_e}{\mu_0} \int_0^{2\pi} B_r B_t d\theta \tag{11}$$

where L_{ef} is the axial length; R_e is a circle of a radius; μ is the permeability of the vacuum; B_r and B_t are the radial and tangential magnetic flux densities, respectively.

Figure 10 shows the output torque of the three motors. From the figure, we can find that the output torque of M3 is much higher than that of M1 and M2. This is because the spoke structure can connect the stators on both the inner and outer sides, so as to make more effective use of the magnetic field line. We can also find that the torque ripple of M2 is lower than that of M1 and M3. This is because the Halbach array can effectively improve the air gap waveform, and thus, the torque ripple is reduced.

Table 2 lists the quantitative comparison of the performance of the three motors. It includes torque, torque ripple, torque density, and power factor.

TABLE 2. Quantitative comparison of motor performance.

	M1	M2	M3
Output torque	97.42 N·m	136.09 N·m	175.53 N·m
Torque ripple	6.44%	5.42%	5.38%
Torque density	29.79 kN·m/m^3	41.62 kN·m/m^3	53.68 kN·m/m^3
Power factor	0.97	0.97	0.97

5. CONCLUSION

In this paper, a comprehensive performance comparison study of DSMFMM with three different magnetization direction of permanent magnets have been investigated. Several conclusions are drawn as follows:

1) According to the principle of magnetic field modulation, the main working harmonics of the three motors are 4th and 23rd. Compared with M1, the two working harmonic amplitudes of M2 and M3 are increased leading to a increase in torque for both M2 and M3.

2) Considering that the saturation of flux line leads to a decrease in the utilization of the permanent magnet, the design parameters of the permanent magnet are selected as optimization variables. When the thickness of the permanent magnet is 2 mm, the performance of the motor is optimal.

ACKNOWLEDGEMENT

This work was supported by the National Natural Science Foundation of China (52477056).

REFERENCES

[1] Shi, Z., X. Sun, Z. Yang, Y. Cai, G. Lei, J. Zhu, and C. H. T. Lee, "Design optimization of a spoke type axial-flux PM machine for in-wheel drive operation," *IEEE Transactions on Transportation Electrification*, Vol. 10, No. 2, 3770–3781, Jun. 2024.

[2] Jing, L., W. Tang, T. Wang, T. Ben, and R. Qu, "Performance analysis of magnetically geared permanent magnet brushless motor for hybrid electric vehicles," *IEEE Transactions on Transportation Electrification*, Vol. 8, No. 2, 2874–2883, Jun. 2022.

[3] Sun, X., N. Xu, and M. Yao, "Sequential subspace optimization design of a dual three-phase permanent magnet synchronous hub motor based on NSGA III," *IEEE Transactions on Transportation Electrification*, Vol. 9, No. 1, 622–630, Mar. 2023.

[4] Shi, Z., X. Sun, G. Lei, X. Tian, Y. Guo, and J. Zhu, "Multiobjective optimization of a five-phase bearingless permanent magnet motor considering winding area," *IEEE/ASME Transactions on Mechatronics*, Vol. 27, No. 5, 2657–2666, Oct. 2022.

[5] Liu, G., H. Zhong, L. Xu, and W. Zhao, "Analysis and evaluation of a linear primary permanent magnet vernier machine with multiharmonics," *IEEE Transactions on Industrial Electronics*, Vol. 68, No. 3, 1982–1993, Mar. 2021.

[6] Wang, Q., F. Zhao, and K. Yang, "Analysis and optimization of the axial electromagnetic force for an axial-flux permanent magnet vernier machine," *IEEE Transactions on Magnetics*, Vol. 57, No. 2, 1–5, Feb. 2021.

[7] Wang, M., C. Tong, Z. Song, J. Liu, and P. Zheng, "Performance analysis of an axial magnetic-field-modulated brushless double-rotor machine for hybrid electric vehicles," *IEEE Transactions on Industrial Electronics*, Vol. 66, No. 1, 806–817, Jan. 2019.

[8] Bai, J., P. Zheng, C. Tong, Z. Song, and Q. Zhao, "Characteristic analysis and verification of the magnetic-field-modulated brushless double-rotor machine," *IEEE Transactions on Industrial Electronics*, Vol. 62, No. 7, 4023–4033, Jul. 2015.

[9] Yoon, K.-Y. and B.-I. Kwon, "Optimal design of a new interior permanent magnet motor using a flared-shape arrangement of ferrite magnets," *IEEE Transactions on Magnetics*, Vol. 52, No. 7, 1–4, Jul. 2016.

[10] Chai, F., J. Xia, B. Guo, S. Cheng, and J. Zhang, "Double-stator permanent magnet synchronous in-wheel motor for hybrid electric drive system," Vol. 45, No. 1, 278–281, Jan. 2009.

[11] Asgar, M., E. Afjei, and H. Torkaman, "A new strategy for design and analysis of a double-stator switched reluctance motor: Electromagnetics, FEM, and experiment," *IEEE Transactions on Magnetics*, Vol. 51, No. 12, 1–8, Dec. 2015.

[12] Li, J., K. T. Chau, J. Z. Jiang, C. Liu, and W. Li, "A new efficient permanent-magnet vernier machine for wind power generation," *IEEE Transactions on Magnetics*, Vol. 46, No. 6, 1475–1478, Jun. 2010.

[13] Wang, H. and S. Ding, "Design and analysis of new dual-stator field modulation machines with multiple magnetic excitations," *IEEE Transactions on Magnetics*, Vol. 57, No. 2, 1–6, Feb. 2021.

[14] Zhu, H., H. Wang, S. Ding, C. He, Z. Li, and S. Chen, "A new staggered dual stator field modulation machine with O-shape permanent magnet excitation," in *2022 Joint MMM-Intermag Conference (INTERMAG)*, 1–5, New Orleans, LA, USA, 2022.

[15] Yue, Y., S. Jia, and D. Liang, "New topologies of high torque density machine based on magnetic field modulation principle," *CES Transactions on Electrical Machines and Systems*, Vol. 7, No. 1, 1–10, Mar. 2023.